Electronic Supplementary Material (ESI) for Sustainable Energy & Fuels.
This journal is © The Royal Society of Chemistry 2017

Deconvoluting the Influences of 3D Structure on the Performance of Photoelectrodes for Solar-Driven Water Splitting

SUPPORTING INFORMATION

Table of Contents

Section ***Page***

I. Photoelectrodeposition of Pt on p-Si MIS photocathodes……………………………………1

II. Cross-sectional TEM ……………………………………………………………………… 3

III. Variation in Ti thickness measured by cross-sectional SEM ………………………...….. 4

IV. Additional SEM images and EDS spectra of as-made micro-pillar samples…………...5

V. Angular dependence of photocurrent in 3D structured samples……………………….... 7

VI. Determining effective diffusion lengths from SPCM……………………………………..8

VII. SPCM images for large pillars………………………………………………………….. 10

VIII. Estimating effective diffusion lengths from EQE measurements…………………......... 11

IX. EBIC measurements………………………………………………………………......... 13

X. Photoelectrode conversion efficiency calculations……………………………………..........15

XI. Procedure for constructing loss analysis figures…………………………………........ 16

I. Photoelectrodeposition of Pt on p-Si MIS photocathodes

Catalytic Pt nanoparticles were electrodeposited onto the surface of Ti-coated p-Si photocathodes from a deposition bath consisting of 3 mM K_2PtCl_4 and 0.5 M NaCl supporting electrolyte, which had a pH of 4. LSV curves carried out in the deposition bath in the dark and under illumination are provided in Figure S1 for two planar photoelectrodes consisting of 10 nm of Ti that was deposited by electron-beam evaporation onto p-Si(100). Both LSV curves are the second of two LSV curves that were recorded under identical scan conditions. LSV curves were

measured at a scan rate of 2 mV s^{-1} and scanned from positive to negative potential. In the dark, the onset of Pt deposition occurs around +0.25 V vs. Ag|AgCl, and the deposition current is seen to continuously increase until a potential of -0.65 V vs. Ag|AgCl. As the applied potential is scanned more negative there is a suppression in deposition current, followed by a subsequent increase in current that can be attributed to the hydrogen evolution reaction (HER). The LSV curve recorded under illumination is qualitatively similar to that recorded in the dark, except that all features have larger current densities and are shifted to more positive potentials ≈ +450 mV. This shift in the Pt deposition onset potential under illumination is very similar to the photovoltage reported for the planar Ti|SiO_2|p-Si MIS photoelectrode in the main article (Figure 8). In this study, Pt nanoparticles were deposited at a constant deposition potential (E_{dep}) of -0.1 V vs. Ag|AgCl under illumination. From a comparison of the current densities recorded at -0.1 V vs. Ag|AgCl, the LSV curves in Figure S1 indicate that Pt deposition occurring at this potential takes place primarily through photoelectrodeposition whereby the electrons involved in Pt electrodeposition are photo-generated minority carriers.

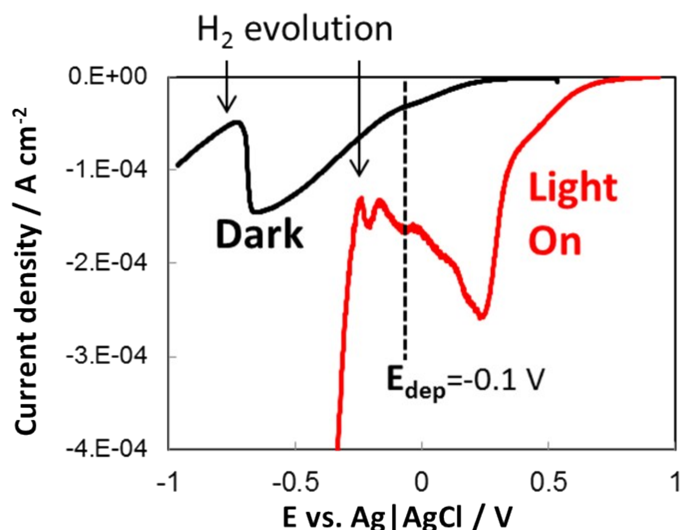

Figure S1. LSV curves for 10 nm Ti/p-Si(100) in the dark and under AM 1.5G illumination (100 mW cm^{-2}) in 3 mM K_2PtCl_4 | 0.5 M NaCl (pH=4) with a scan rate of 2 mV s^{-1}.

II. Cross-sectional TEM

A 10 nm or 15 nm Ti layer was deposited by e-beam evaporation onto all of the samples used in this study. The deposition was conducted under planetary rotation, which assists in depositing the Ti metal over the whole surface of the 3D structured samples, even on the sidewalls. Despite planetary rotation, non-uniform deposition rates still occur due to uneven shading by the pillar structures, resulting in varying Ti layer thickness. Cross-sectional transmission electron microscopy (TEM) was attempted for a standard 3D MIS sample in order to better view the structure of the platinum-titanium-silica-silicon junction and Pt particles at various locations on the sample. Figure S2 contains cross-sectional TEM images of the MIS junction on the top of a pillar, revealing numerous Pt particles sitting on top of the SiO_2/TiO_x bilayer. The Pt particles seen in this image have a fairly porous structure, closely resembling the structure of electrodeposited Pt particles observed by Ustarroz et al.[1] Unfortunately, difficulties in sample preparation prevented attainment of useful cross-sectional TEM images of the MIS junction at the pillar sidewalls and basal region.

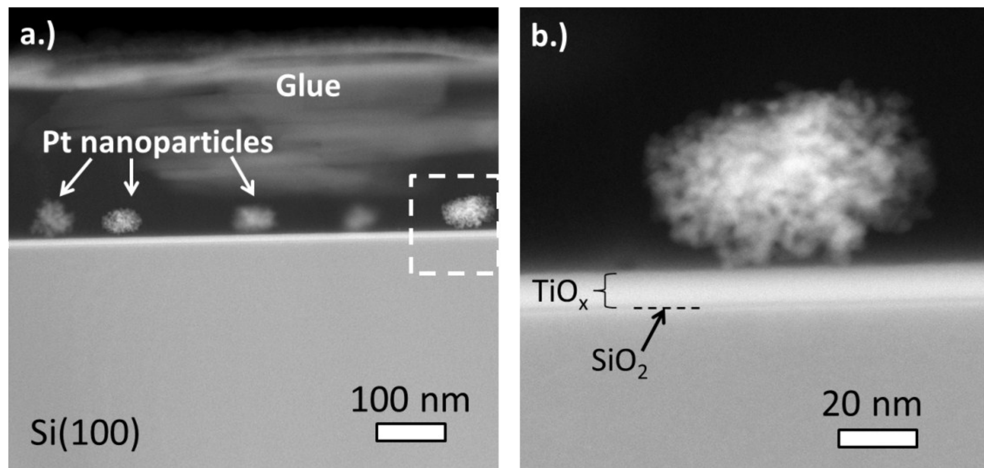

Figure S2. Cross-sectional TEM images of the top surface of a pillar. Figure b.) shows a higher magnification view of the particle that is identified by the dashed rectangle in Figure S2a.

III. Variation in Ti thickness based on cross-sectional SEM

In the absence of high quality TEM images of pillar sidewalls, scanning electron microscopy (SEM) was used to estimate the variation in the thickness of the e-beam deposited Ti layer by intentionally depositing a thick Pt/Ti bilayer (total thickness ≈ 140 nm) onto a 3D structured sample. After cleaving the sample, cross-sectional SEM was used to measure the relative thickness of the deposited metal bilayer on the pillar top, side-wall, and basal regions. SEM images of one such pillar that was split in half is shown in Figure S3, revealing that the metal thickness on the pillar sidewall is 65 % lower than that deposited on the pillar tops and basal regions. If it is assumed that the same top/sidewall thickness ratio is also obtained for the thinner Ti layer deposited for the main samples in this study, then the thickness of the Ti layer deposited on the sidewall is expected to be ≈5 nm if the deposition thickness on the top is 15 nm. Although we were not able to directly determine the Ti layer thickness on the side-wall by TEM, Energy Dispersive X-Ray Spectroscopy measurements verified that Ti was indeed present (section IV).

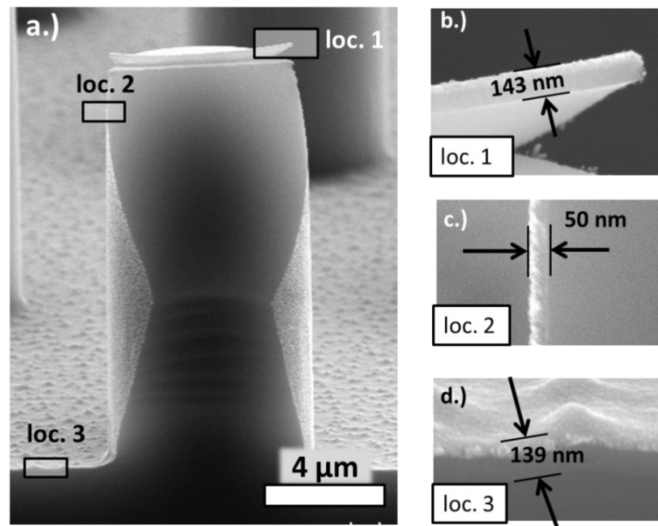

Figure S3. Cross-sectional SEM image of a Si micropillar onto which a "thick" Pt/Ti bilayer was deposited by e-beam evaporation as a means to estimate the thickness ratio of the metal layer on the pillar top and sidewalls. In Fig. S3b, the metal layer on the pillar top delaminated when the sample was cleaved.

IV. Additional SEM images and EDS spectra of as-made micro-pillar samples

Figure S4 contains SEM images of an as-synthesized Si micropillar sample that show the presence of a high density of electrodeposited Pt nanoparticles on the top, sidewall, and basal areas. The bright appearance of the pillar top and darker appearance of the pillar side wall and basal regions is an artifact of self-shadowing of the back scattered and secondary electrons due to the relative positions of the electron gun and SEM detector with respect to the 3D structures.

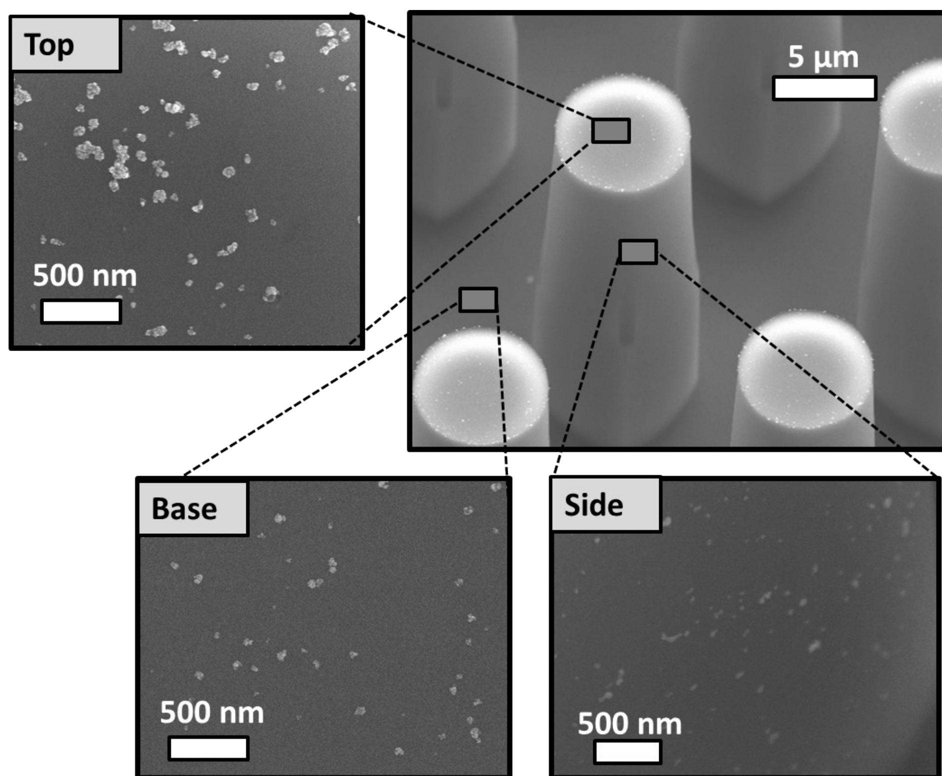

Figure S4. Low-resolution SEM image of as-synthesized Si micropillar (upper left) and high resolution images that show electrodeposited Pt nanoparticles on the pillar top, side-wall, and basal region. Scale bars in the top right figure are valid for the x dimension only.

Although larger Pt particles could be observed directly on side-walls by SEM, the presence of the thin e-beam deposited Ti layer on the pillar side walls was confirmed by Energy Dispersive X-Ray Spectroscopy (EDS). An EDS spectrum of the side-wall of a Si micropillar is shown in Figure S5, showing a distinct Ti Kα peak.

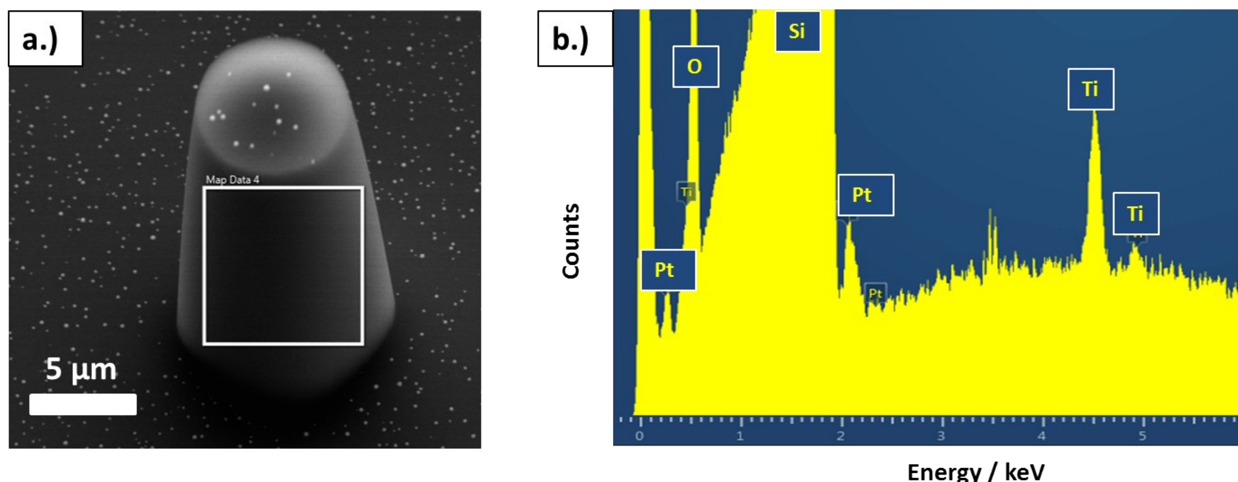

Figure S5. a.) SEM image and b.) EDS spectra of as-synthesized MIS Si micropillar that shows the presence of Pt and Ti on the pillar sidewalls. The white box in a.) indicates the region where the EDS spectrum was measured. The scale bar in the SEM image is only applicable to the x dimension.

In Figure S6, higher resolution SEM images of a typical as-fabricated Si micropillar shows noticeable nanoscale etch damage on the pillar side-walls, but not the pillar tops. Roughness could be observed on the basal surfaces between pillars (see Figure S2a,d).

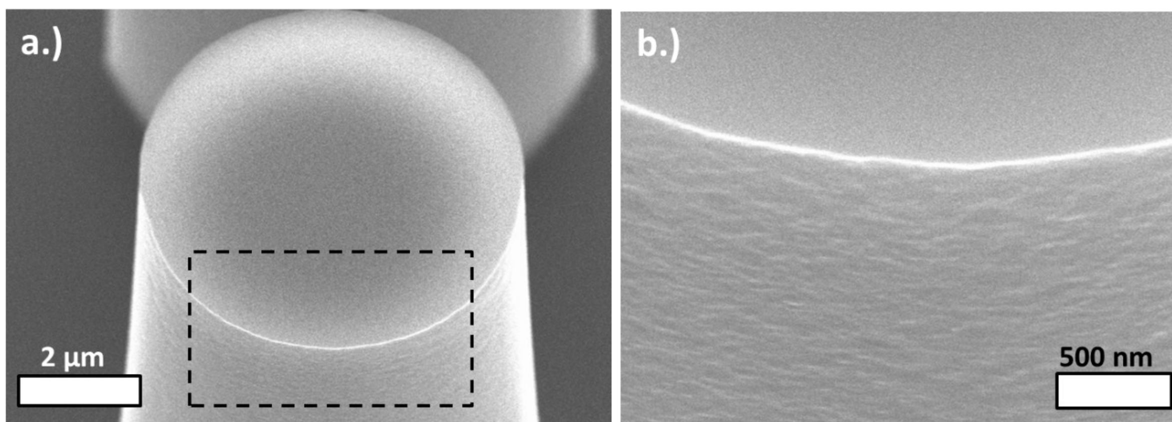

Figure S6. SEM images of Si micropillar after RIE fabrication and rapid thermal annealing but before metal deposition. Image in b.) shows high resolution view of area marked in box in a.). Scale bars apply only to the x dimension in the SEM images.

V. Angular dependence of photocurrent in 3D structured samples

An important optical consideration for photoelectrode operation is the angular dependency of the reflectance. For a perfectly flat electrode, the power of incident light, P, is given by the product of the incident irradiance, P_o, the projected illuminated surface area, A_{hv}, and the transmittance, $(1-R(\theta))$:

$$P = P_o \cdot A_{hv} \cdot (1 - R(\theta)) = P_o \cdot A_{2D} \cdot cos(\theta) \cdot (1 - R(\theta)) \quad \text{(S1)}$$

where θ is the incident angle with respect to the surface normal. For smooth planar surfaces, reflectance is relatively independent of incident angle, meaning that P decreases significantly as θ increases. However, the reflectance of 3D structured solar cells can decrease with θ_i, helping to offset the $\cos(\theta_i)$ term in Equation S1. The angular-dependency of reflection is evident in a series of photographs of a 3D-structured photoelectrode taken with the camera positioned at different angles with respect to the sample surface normal (Fig S6a). As the incident angle increases, a higher percentage of the incident light becomes incident on the pillar side-walls. This light is more likely to be absorbed or scattered than light incident on the pillar tops or inter-pillar surfaces, resulting in decreased R and a darker appearance of the photoelectrode surface. More importantly, decreased R means that a higher percentage of incident light can be absorbed and converted into photocurrent by the 3D structured photoelectrode than the planar control.

To illustrate this effect, the limiting photocurrents of a planar and micro-pillar array p-Si photoelectrode were measured under simulated AM 1.5G illumination as a function of the incident angle. The photocurrent normalized to the exposed 2D electrode area (A_{2D}) is plotted in Figure S7b, while the photocurrent normalized by the projected 2D area of illumination (A_{hv}) is shown in Figure S7c. Comparison of these curves reveals that the photocurrent densities of these two samples are similar at normal incidence, but the photocurrent of the 3D structured

micropillar photoelectrode is substantially greater at larger incident angles. The difference is especially pronounced when normalized to the projected illuminated area of the photoelectrode, an observation that is consistent with higher degree of scattering and absorption of light by the 3D structured electrode at wider incident angles. The increased photocurrent made possible by 3D structuring at wider incident angles in Figure S7 would amount to a significant amount of increased H_2 production over the course of the day. Such behavior has previously been reported for a number of 3D photoelectrodes.[2]

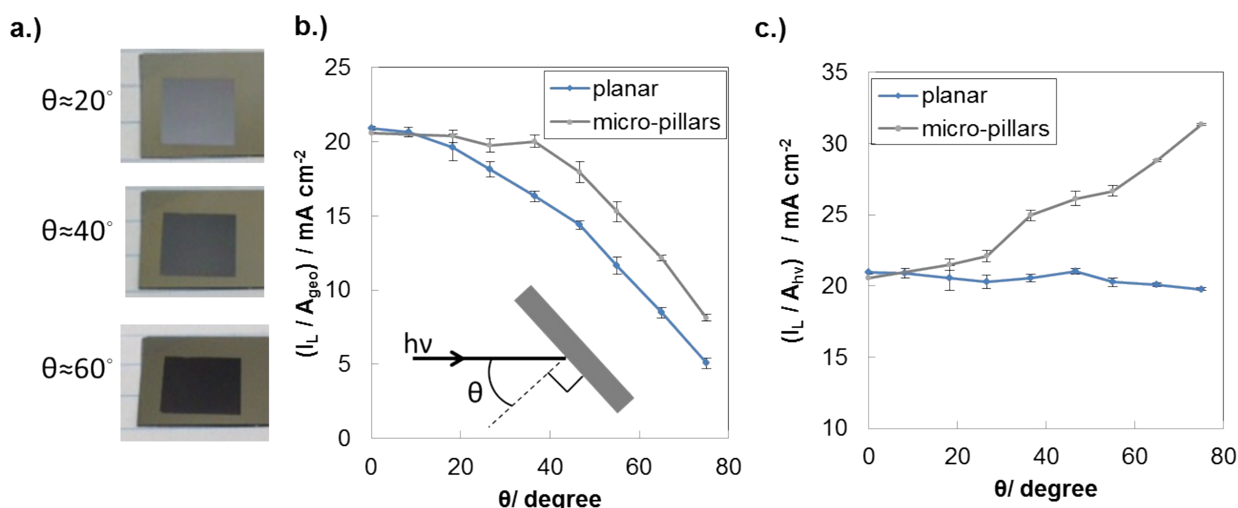

Figure S7. a.) Optical photographs of a photoelectrode containing micropillar arrays that is viewed from three different angles with respect to the surface normal (θ). b.), c.) Limiting photocurrent densities (j_L) of a planar and 3D-structured photoelectrode as a function of the incidence angle (θ) of a collimated AM 1.5G light source. The total recorded limiting photocurrent (I_L) was divided by the 2D exposed electrode surface area (A_{geo}) in b.) and by the projected 2D illuminated area (A_{hv}) in c.). In order to avoid the influence of bubbles, I_L values were obtained as an average of three separate LSV curves measured successively in deaerated 0.5 mol L^{-1} H_2SO_4 at 100 mV s^{-1}. Error bars are based on a 95 % confidence level.

VI. Determining effective diffusion lengths from SPCM

In SPCM, photocurrent produced in the sample is analyzed as a function of the position of a localized excitation source, typically a focused laser beam. The position of the localized excitation is adjusted by a nano- or micro-positioner that controls either the sample stage or

optics. For determining the effective diffusion length of minority carriers in solid-state p-n or MIS junction solar cells, SPCM in dry environment can be used. In these experiments, PtTi contact pads were evaporated onto the surfaces of two planar SiO_2/p-Si(100) samples, one which underwent RIE treatment alongside 3D samples, and one which did not. The PtTi contacts were then contacted by a Tungsten probe, and the photocurrent (J_{ph}) collected across the MIS junction was measured as a function of laser beam distance from the edge of the contact (D_L). The laser beam induced photocurrent was recorded as a function of D_L, and effective diffusion length (L_e) was calculated from a plot of the logarithm of the normalized photocurrent, $\ln(J_N)$, versus D_L:

$$L_e = -\left(\frac{d\ln J_N}{dD_L}\right)^{-1} \tag{S2}$$

As determined from the data in Figure S8, the values of L_e for the RIE- and non-RIE processed samples are provided in Table SI. The large difference in L_e values between these two samples highlights the detrimental influence of the RIE processing steps on bulk and/or surface recombination for the Si micropillar arrays.

Table SI. Values of L_e determined by SPCM using 790 nm and 532 nm lasers. Uncertainty intervals are based on Student's t 95 % confidence level, and are based on multiple line scans on multiple contact pads.

	L_e / μm	
Sample	measured at 532 nm	measured at 790 nm
RIE-processed device	12.1 ± 1.0	12.2 ± 0.9
non-RIE processed device	61.4 ± 3.1	64.3 ± 5.0

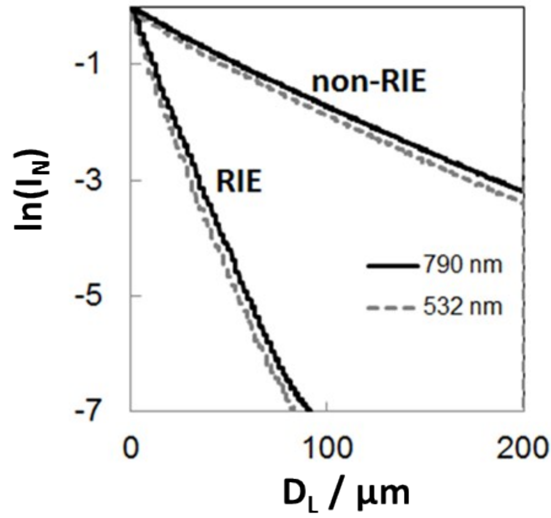

Figure S8. Dry SPCM measurements used to determine the effective minority carrier diffusion length (L_e) in planar c-Si MIS photoelectrodes with and without RIE treatment to the surface. Laser spot sizes for these measurements were ≈ 3 µm and with laser powers of 3.69 µW (for 532 nm laser) and 1.79 µW (for 790 nm laser).

VII. SPCM images for large pillars

Figure S9 contains SPCM line scans and photocurrent images that were performed on three Si micropillars having varying radii. For both line scans and images, a 790 nm laser beam was used as the source of illumination, and the measured photocurrent was normalized to that which was measured in the basal areas in between the pillars, which serve (locally) as a planar control. As shown in the main article, the small radius (r) pillar exhibits a uniform enhancement in photocurrent with the 790 nm laser beam that is independent of laser position on the top of the pillar. By contrast, the photocurrent for the pillars with larger radii, for which $r > (L_e + W) \approx 12$ µm, exhibit a significant dip in the photocurrent when the laser beam is positioned in the center of the micropillar. For the largest pillar (r = 40 µm), the local photocurrent at the center of the pillar is found to be nearly equal to that for which the laser beam is positioned on the planar region completely off of the pillar.

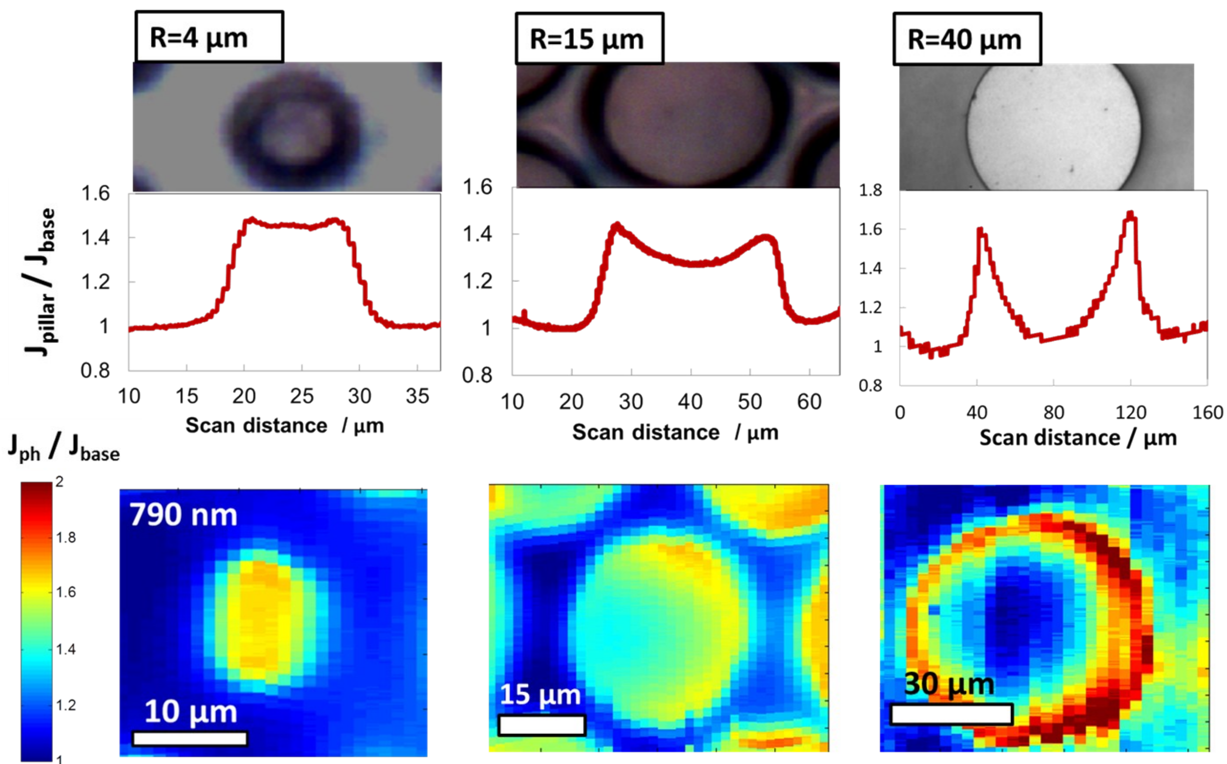

Figure S9. Dry SPCM line scans and images of 27 µm tall MIS Si micropillar samples of different radii. Measurements were performed with 790 nm laser beam (spot size ≈ 4 µm, power = 4 µW) in 0.5 mol L^{-1} H_2SO_4 at an applied potential of −50 mV vs. RHE.

VIII. Estimating effective diffusion lengths from EQE measurements

External quantum efficiency (EQE) spectra of planar and 3D structured photoelectrodes were computed as follows. First, the power of the incident monochromatic light, $P_o(\lambda)$, was measured as a function of wavelength using a National Institute of Standards and Technology-traceable Si photodiode. Next, the photocurrent, $I(\lambda)$, was recorded in 0.5 mol L^{-1} H_2SO_4 as a function of wavelength under an applied potential of −0.22 V versus Ag/AgCl. Under the low light intensity of the monochromatic light, this potential corresponded to the limiting current region of the LSV curve. Knowing both $P_o(\lambda)$ and $I(\lambda)$, the EQE spectra were calculated from Equation (S3):

$$EQE(\lambda) = \frac{\left(\frac{I(\lambda)}{q}\right)}{\left(P_o(\lambda)\cdot\frac{\lambda}{h\cdot c}\right)} \tag{S3}$$

where h is the Planck constant, c is the speed of light, q is the elementary charge, and $I(\lambda)$ is the measured photocurrent.

EQE spectra were used to estimate the effective minority carrier diffusion length (L_e) of photoelectrodes by fitting a Gartner carrier collection model (Eqn. S4) to the long wavelength section of the experimental quantum efficiency (QE) spectrum. At longer wavelengths, the absorption depth of light is on the same order of magnitude as the collection length, ($L_e + W$), and therefore is highly sensitive to L_e. The internal quantum efficiency (IQE) can be modeled as a function of wavelength (λ) :[3, 4]

$$IQE \cong 1 - \frac{exp(-\alpha(\lambda)\cdot W)}{\alpha(\lambda)\cdot L_e + 1} \tag{S4}$$

where $\alpha(\lambda)$ is the semiconductor absorption coefficient and W is the depletion width. In this study, the wavelength-dependent absorption coefficient data for c-Si were used from literature,[5] and a depletion width of $W = 2$ µm was used based on the resistivity of the p-Si wafers used in this study (1 Ω·cm to 5 Ω·cm).[6] For this analysis, the experimental IQE spectrum was taken to be equal to the EQE normalized to the maximum EQE value (EQE_{max}) at short wavelengths, a valid assumption if photocurrent losses at EQE_{max} are primarily due to optical reflection from the photoelectrode surface and/or absorption by the solution.[4] Figure S10 shows plots of the normalized EQE (EQE_{norm}) spectrum for the planar RIE and 3D MIS sample with highest pillar density, along with the modeled IQE spectrum according to Equation S4. Based on a least

squares regression fit of L_e to the experimental EQE_{norm} data over the range 800 nm < λ < 980 nm, values of L_e of 11 μm and 27 μm were determined for the planar and 3D MIS samples, respectively. Although the fitted value of L_e for the planar sample is in good agreement with that determined from SPCM (Table S1), the fitted value of L_e for the 3D photoelectrode is very similar to the height of the micropillars, and can be explained by enhanced carrier collection. The quality of the fit for the 3D photoelectrode likely suffers due to the heterogeneous nature of the micropillar sample.

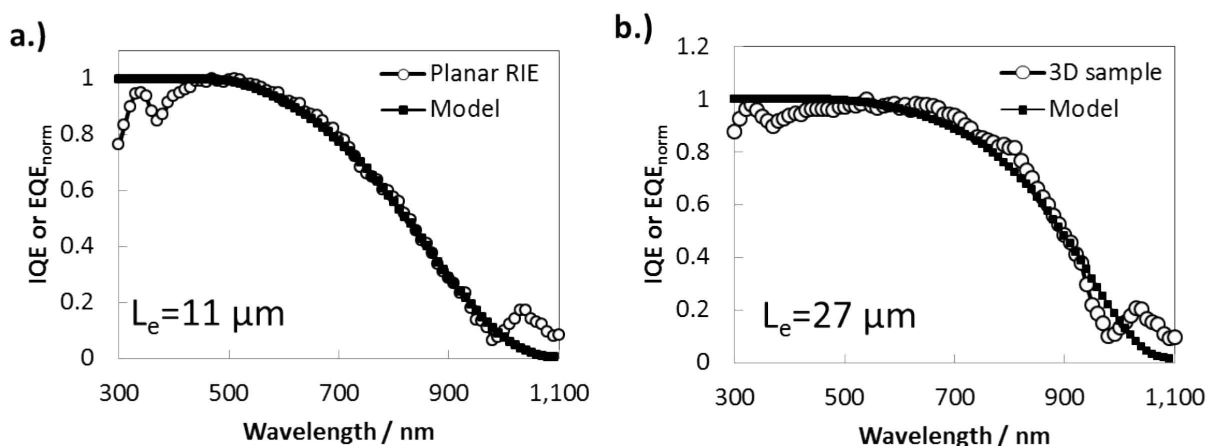

Figure S10. Experimental normalized EQE spectra and modeled IQE spectra for the planar RIE photoelectrode 3D structured photoelectrode with highest pillar density used in this study. The modeled IQE spectra were fit to the experimental data over the range of 800 nm < λ < 980 nm using a least squares regression in which L_e was the only parameter that was adjusted. Experimental EQE spectra were taken at an applied potential of −0.22 V Ag/AgCl (≈ 0.0 V vs. RHE) in deaerated 0.5 mol L^{-1} H_2SO_4.

IX. EBIC measurements

This section describes the model that leads to Equation (5) of the main text and is used to model the influence of surface recombination in the radial geometry. This model follows an approach the was previously outlined in literature.[7] We first consider diffusion in radial coordinates (ρ,ϕ).

Assuming the system is invariant with respect to azimuthal angle ϕ, we arrive at the continuity equation for the density $n(\rho,t)$ as a function of radial position ρ and time t:

$$\frac{\partial n(\rho,t)}{\partial t} = -\frac{1}{\rho}\frac{\partial}{\partial \rho}\left[\rho j_{\rho}\right] - \frac{n(\rho,t)}{\tau_{bulk}} \tag{S5}$$

where $j_{\rho} = D \partial n / \partial \rho$ is the radial diffusion current. Following the standard separation of variables approach, we let $n(\rho,t) = T(t) \times N(\rho)$ and find the following equations for $T(t)$ and $N(\rho)$:

$$\frac{\partial T(t)}{\partial t} = -\left(\frac{1}{\tau_{bulk}} + \lambda\right) T(t) \tag{S6}$$

$$D\frac{1}{\rho}\frac{\partial}{\partial \rho}\left[\rho \frac{\partial N(\rho)}{\partial \rho}\right] = \lambda N(\rho) \tag{S7}$$

where λ is a constant arising from separation of variables. We will see shortly that λ is determined by the boundary conditions; physically, λ modifies the carrier lifetime, as indicated by the right hand side of Eq (S6). The boundary conditions for Equation (S7) are:

$$j_{\rho}(0) = 0 \tag{S8}$$

$$j_{\rho}(r) = S \times n(r) \tag{S9}$$

The solution of Equations (S7-S8) is $N(r) \propto J_0(r\sqrt{\lambda/D})$, where J_0 is the order 0 Bessel of the first kind. Plugging this solution into Eq. (S9) yields the following equation for λ:

$$\sqrt{\lambda D}\, J_1(r\sqrt{\lambda/D}) = S\, J_0(r\sqrt{\lambda/D}) \tag{S10}$$

In the limit $S \gg D/r$, an explicit solution to Equation (S10) is given by Equation (5) in the main text. More generally, Equation (S10) requires numerical solution. We have checked that the approximations leading to the analytical formula given in the main text apply to our systems.

X. Photoelectrode conversion efficiency calculations

The photoelectrode conversion efficiencies, η_{PE}, of the planar RIE and 3D structured photoelectrodes discussed in loss analysis section of the main article were calculated from:

$$\eta_{PE} = \left[\frac{|I_{ph}|(\Delta E - |V_{b,ideal}|)}{P_{hv}}\right] \tag{S11}$$

where ΔE is the thermodyanmic cell voltage for water electrolysis corresponding to the difference between the reversible potentials for the HER ($E_{H+/H2}$) and OER ($E_{O2/H2O}$) half reactions, I_{ph} is the operating photocurrent density, and P_{hv} is the net irradiance of the incident light (100 mW cm^{-2} for the simulated AM 1.5G light source in this work). I_{ph} was set equal to I_{mpp}, the photocurrent density at the maximum power point (mpp) of the LSV curve corresponding to the point on the LSV curve where the product of the photocurrent and the applied potential with respect to the reversible hydrogen electrode (RHE) are maximized, as shown in Figure S11. Because photovoltages generated by the photocathodes in this work do not exceed ΔE, a bias voltage (V_b) must be applied between the photocathode and the counterelectrode. In this work, η_{PE} was calculated from 3-electrode LSV measurements and assuming that the bias voltage, $V_{b,ideal}$, is that required to split water using an ideal, non-polarized counterelectrode that has no kinetic overpotential losses. In this case, the term (ΔE - $V_{b,ideal}$) in

Equation S11 is equal to the operating potential of the photoelectrode at the maximum power point defined above. The above definition of η_{PE} is very similar to the applied bias photon-to-current conversion efficiency (ABPE),[8] which is typically determined from a 2-electrode measurement that includes losses at the counterelectrode. In Equation S11, the assumption of an ideal, nonpolarized counterelectrode ensures that the photoelectrode conversion efficiencies reported here represent a figure of merit for the photoelectrode that is independent of the size and material used for the counterelectrode.[9] LSV curves used for these efficiency calculations were first IR-corrected to remove series resistance associated with the indium solder back contacts and solution resistance and thereby provide a more accurate comparison between samples.

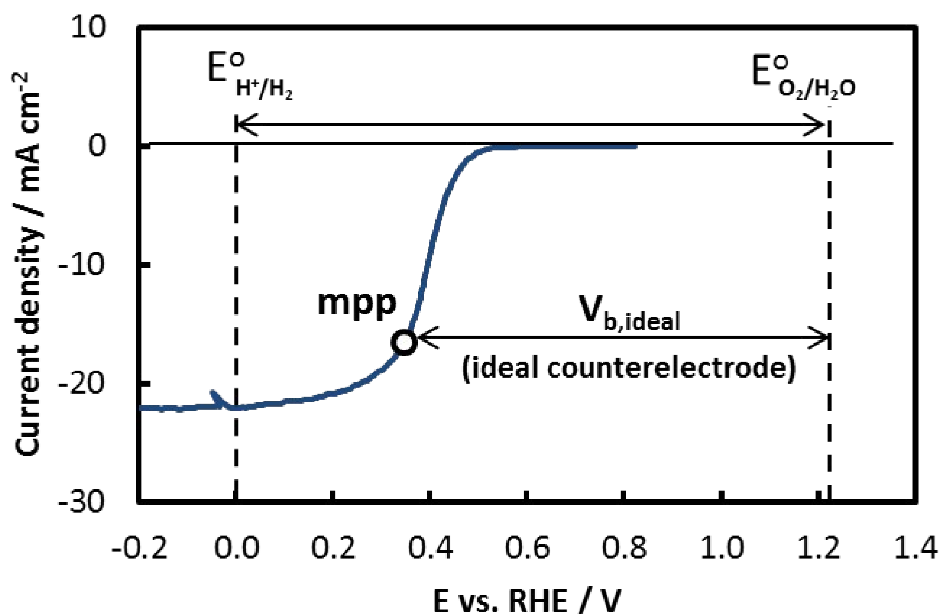

Figure S11. Schematic illustrating how the photoelectrode conversion efficiency was calculated from *IR*-corrected LSV curves of the p-Si MIS photocathodes in this work.

XI. Procedure for constructing loss analysis figures

The photoelectrode loss analysis figures included in Section 3.6 of the main article were constructed as follows:

i. ***Solid-state IV behavior:*** The solid-state current-voltage (IV) curve was modeled using the diode equation (Equation 1). The curve represents the photoelectrode IV curve characteristics in the absence of any kinetic, ohmic, or mass transfer losses. The experimentally measured limiting photocurrent from PEC LSV curves in Figure 2 was used as I_L, and the values of n and j_o were obtained from the analysis of photovoltage measurements described in Section 3.5.4. A_j was set equal to the A_{3D} based on the sample's micropillar geometry.

ii. ***Kinetic overpotential losses:*** The kinetic overpotential losses associated with the HER were modeled with the Tafel Equation, Equation (12), using Tafel parameters obtained from semi-empirical correlations between Pt particle coverage (θ_{Pt}), catalytically active surface area (A_{cat}), the effective Tafel slope (β_{eff}), and the effective exchange current density ($i_{o,eff}$). These correlations are shown in Figure S12 and were obtained for a series of metallic control samples consisting of various loadings of Pt particles that were electrodeposited onto 15 nm Ti on conductive p+Si substrates. Because these control samples are metallic in nature, overpotentials recorded in their iR-corrected current-potential curves can be directly assigned to kinetic and/or mass transfer losses.

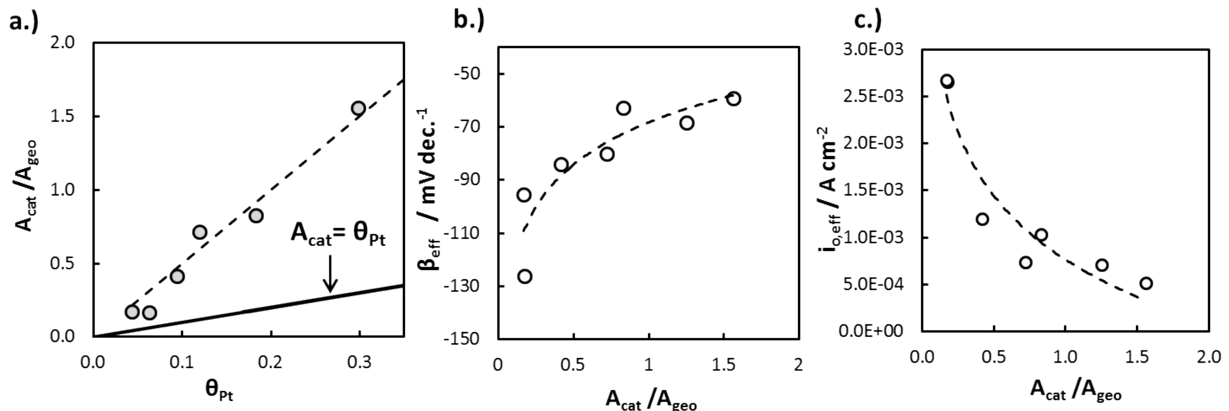

Figure S12. Empirical correlations for control samples of electrodeposited Pt particles on Ti|p$^+$Si substrates used to model the HER kinetic overpotential losses of Pt particles on Pt|Ti|p-Si MIS photoelectrodes. a.) Relationship between the catalytically active surface area (A_{cat}) determined from H_{upd} measurements and the 2D coverage of electrodeposited Pt particles (θ_{Pt}) determined

from three SEM images of each sample. Correlations between A_{cat} and b.) the effective Tafel slope (β_{eff}, mV per decade of current) and c.) the effective exchange current density ($i_{o,eff}$). β_{eff} and $i_{o,eff}$ were determined by fitting the experimental η_{HER} vs. log(I) data to the Tafel equation between 1 mA cm^{-2} and 30 mA cm^{-2}. The dashed line in a.) is a linear fit forced to go through the origin, while the dashed lines in b.) and c.) are fitted curves of the form: $y=C_1\ln(x)+C_2$.

Values of θ_{Pt} were determined from analysis of SEM images for each sample. A_{cat} was taken to be the electrochemically active surface of Pt particles determined from the hydrogen underpotential deposition (H_{upd}) charge measured by cyclic voltammetry in dearated 0.5 mol L^{-1} H_2SO_4 and calculated based on a H_{upd} charge of 210 μC cm^{-2} for polycrystalline Pt.[10] β_{eff} and $i_{o,eff}$ values shown in Figure S12a and S12b were determined from linear fits of the experimental Tafel curves (η_{HER} vs. log(I)) for each Pt|Ti|p^+Si sample in the range of 1 mA cm^{-2} to 30 mA cm^{-2} to the Tafel Equation. It must be emphasized that the effective Tafel slope and exchange current density values obtained from this fitting procedure at higher current densities are different from the "true" Tafel parameters that are linked to fundamental rate constants and reaction mechanisms in the absence of mass transfer limitations. Indeed, it is well-known that mass transport limitations become rate limiting for fast reactions such as the HER in acidic electrolytes, even when measurements are performed with a rotating disk electrode.[11] Instead, the *effective* Tafel parameters reported in Figure S12 are meant to provide a semi-empirical framework based on the Tafel Equation for modeling η_{HER} vs. current density as a function of Pt particle loading.

In this study, the kinetic overpotential losses shown in the loss analysis figures in Section 3.6 were modeled with the Tafel equation using values of A_{cat}, β_{eff}, and $i_{o,eff}$ obtained from the correlations provided in Figure S12 based on the SEM-determined Pt particle coverages of the planar and 3D MIS photoelectrodes. In this analysis, it was assumed that the HER

overpotential losses for the Pt particles electrodeposited onto the Ti|p-Si photoelectrodes are the same as those measured on the Ti|p$^+$Si control samples.

iii. ***Ohmic losses:*** In the absence of the experimental values for the total ohmic resistance, R_Ω, the value of this parameter was fitted as the only unknown parameter in Equation (3) to achieve a least squares fit of the modeled LSV curve to the experimentally measured LSV curve. By multiplying the fitted value of R_Ω by the total current at each point on the IV curve, the ohmic iR-loss "wedge" was determined. The fitted values of R_T were 38.6 Ω and 34.5 Ω for the planar and 3D structured samples, respectively. For this fit, the kinetic losses, $\eta_{cat}(I)$, were modeled as described above and $\phi(I)$ was taken to be zero.

iv. ***Recombination losses:*** The loss in photocurrent in the photo-limiting current regimes of the loss analysis diagram was calculated based on the experimentally-measured effective minority carrier diffusion lengths (Section VI of this document) and the known geometry of the electrodes based on SEM characterization. Using the same procedure and assumptions described in section 2.5.2 of the main article (used to generate Figure 4b,c), the photocurrent losses associated with recombination of minority carriers generated further than (L_e+W) away from the MIS junction were calculated for a normal-incident AM1.5G light source. These calculated losses in the photo-limited regime were equal to 8.8 mA cm^{-2} for the planar photoelectrode, and 6.5 mA cm^{-2} for the 3D photoelectrode. As described below, these values were then used to determine the magnitude of the optical losses, which can be assumed to be independent of applied potential. Therefore, at potentials more positive than the limiting photocurrent regime, the carrier recombination losses can be taken to be given by the difference between the ideal diode i-E curve and the optical loss wedge.

v. ***Optical losses:*** The maximum theoretical photocurrent for c-Si under AM 1.5G illumination, $j_{\mathrm{max,Si}}$, was calculated based on the standard AM 1.5G spectrum and optical properties of c-Si.[5] The optical losses wedge, which accounts to losses due to reflection from the front of the photoelectrode and absorption by the Ti overlayer and Pt nanoparticles, was taken to be equal to the difference between $j_{max,Si}$ and the sum of the experimentally-observed photo-limiting current and calculated bulk carrier recombination losses described in the preceding paragraph. As described in section 2.5.1 of the main article, direct measurement of these optical losses was not achieved in this study, but would be preferred in future studies.

Supporting Information References

1. J. Ustarroz, T. Altantzis, J. A. Hammons, A. Hubin, S. Bals and H. Terryn, *Chemistry of Materials*, 2014, **26**, 2396-2406.
2. S. W. Boettcher, E. L. Warren, M. C. Putnam, E. A. Santori, D. Turner-Evans, M. D. Kelzenberg, M. G. Walter, J. R. McKone, B. S. Brunschwig, H. A. Atwater and N. S. Lewis, *J. Am. Chem. Soc.*, 2011, **133**, 1216-1219.
3. X. X. Liu and J. R. Sites, *Journal of Applied Physics*, 1994, **75**, 577-581.
4. J. R. McKone, A. P. Pieterick, H. B. Gray and N. S. Lewis, *J. Am. Chem. Soc.*, 2013, **135**, 223-231.
5. M. A. Green and M. J. Keevers, *Progress in Photovoltaics*, 1995, **3**, 189-192.
6. E. H. Rhoderick and R. H. Williams, in *Metal-Semiconductor Contacts*, Clarendon Press, Oxford, second edn., 1988, ch. 252, p. 252.
7. J. E. Allen, E. R. Hemesath, D. E. Perea, J. L. Lensch-Falk, Z. Y. Li, F. Yin, M. H. Gass, P. Wang, A. L. Bleloch, R. E. Palmer and L. J. Lauhon, *Nat. Nanotechnol.*, 2008, **3**, 168-173.

8. Z. Chen, H. N. Dinh and E. Miller, *Photoelectrochemical Water Splitting Standard, Experimental Methods, and Protocols*, Springer, 2013.

9. G. Hodes, *Journal of Physical Chemistry Letters*, 2012, **3**, 1208-1213.

10. S. Trasatti and O. A. Petrii, *Pure and Applied Chemistry*, 1991, **63**, 711-734.

11. W. C. Sheng, H. A. Gasteiger and Y. Shao-Horn, *Journal of the Electrochemical Society*, 2010, **157**, B1529-B1536.